Uncertainty-Aware Optimization of Electricity–Gas–Heat–Hydrogen Hubs with Behind-the-Meter Systems for Cost and Emissions Reduction

Ali Ahmadian[1,*] and Farshid Azizi[1,2]

[1] *Department of Electrical Engineering, University of Bonab, Bonab, Iran*
[2] *Eastern Azarbaijan Electric, Power Distribution Company, Tabriz, Iran*
**Corresponding author: ali.ahmadian1367@gmail.com*

Manuscript received 28 June, 2026; revised 27 August, 2026; accepted 12 September, 2026. Paper no. JEMT-2606-1604.

This study develops a robust scheduling framework for an integrated electricity–gas–heat–hydrogen energy hub with Behind-the-Meter (BTM) photovoltaic–battery systems and multi-carrier demand response. The framework jointly represents renewable-generation and electrical, gas, and heat demand uncertainties through polyhedral uncertainty sets, while incorporating battery degradation-aware operating constraints and technology-specific emissions. Four configurations are evaluated under common system conditions to isolate the effects of BTM resources and demand response. The baseline operating cost of $14,528 decreases to $11,281 with BTM resources, $13,661 with demand response, and $9,650 when both are coordinated, corresponding to a maximum cost reduction of 33.6%. Emissions decrease from 14,805 kg CO_2e in the baseline to 14,115 kg CO_2e with BTM resources, whereas demand response alone increases emissions to 15,383 kg CO_2e. Their combined operation limits emissions to 14,239 kg CO_2e while achieving the lowest operating cost. The results show that the economic and environmental effects of demand-side flexibility depend strongly on its coordination with local generation and storage under uncertainty.

Keywords: *Multi-carrier energy systems, Energy storage degradation, Emissions reduction, Robust optimization, Behind-the-meter systems.*

http://dx.doi.org/10.22109/jemt.2026.588968.1604

Nomenclature

t	Index of Time
CUP	Cost of Power Purchase from Upstream Grid
PUP	Purchased Power from Upstream Grid
GGW	Amount of Gas Purchased from Gas Network
CGW	Cost of Gas Purchase from Gas Network
PG	Local Generator Output
CG	Cost of Generation by Local Generator
SUG	Start-Up Cost of Generator
SDG	Shutdown Cost of Generator
$PCHP$	CHP Output
$CCHP$	Cost of CHP Generation
$SUCHP$	Start-Up Cost of CHP
$SDCHP$	Shutdown Cost of CHP
$PPV2C$	Direct Solar Power Consumed by Local Load
$PPV2ES$	Solar Power Transferred to Storage
$PESS2C$	Power Discharged from Storage to Consumer
$CG2C$	Cost of Supplying Load from Local Grid
$PG2C$	Cost of Energy Exchange Between Grid and Storage
$CPV2G$	Price of Selling Solar Power to Grid
$PPV2G$	Solar Power Sold to Grid
PG_{min}	Minimum Local Generator Power Output
PG_{max}	Maximum Local Generator Power Output
$HCHP$	CHP Unit Thermal Output
$HCHP_{min}$	Minimum CHP Unit Output
$HCHP_{max}$	Maximum CHP Unit Output

$\eta HCHP$	Thermal Efficiency of CHP Unit
$\eta ECHP$	Electrical Efficiency of CHP Unit
ψ	Positive Large Coefficient for Activating Binary Condition
$bvCHP$	Status of CHP Unit On/Off
ηTB	Boiler Efficiency
$PEHP$	Thermal Pump Power Consumption
$\underline{PEHP}$	Minimum Thermal Pump Power Consumption
$\overline{PEHP}$	Maximum Thermal Pump Power Consumption
$HEHP$	Thermal Output of Thermal Pump
σ	Allowed Boiler Power Change Rate
$\sigma P2G$	P2G Equipment Ramp Rate
$\eta P2G$	P2G Equipment Efficiency
$GP2G$	Output Power of Synthetic Gas from P2G Process
$PP2G$	Input Electrical Power to P2G Unit
$\underline{PP2G}$	Minimum Allowed Input Power to P2G Unit
$\overline{PP2G}$	Maximum Allowed Input Power to P2G Unit
δGW	Emission Rate of Gas Received from Network
δCHP	Emission Rate of CHP Unit
δG	Emission Rate of Local Generators
δGT	Gas Turbine Emission Rate
δGB	Gas Boiler Emission Rate
PGT	Gas Turbine Output
ηGT	Gas Turbine Efficiency
PPV^C	Power Generated from Photovoltaic to Local Load in BTM
PPV^{ES}	Discharged Power from Storage to Local Load in BTM
PES^C	Purchased Power from Grid to Local Load in BTM
PG^C	Discharged Power to Grid from Storage in BTM
PG^{ES}	Power Generated from Solar Cells in BTM
P^{WT}	Wind Turbine Output
P^{PV}	Solar Cell Output
ξ	Uncertainty scaling coefficient
P^{Load}	Electrical demand
G^{Load}	Gas demand
H^{Load}	Thermal demand
$P^{\tilde{L}oad}$	Midpoint (reference value) of the electrical-demand uncertainty interval
$P^{\hat{L}oad}$	Half-width of the electrical-demand uncertainty interval
$G^{\tilde{L}oad}$	Midpoint (reference value) of the gas-demand uncertainty interval
$G^{\hat{L}oad}$	Half-width of the gas-demand uncertainty interval
$P^{\tilde{W}T}$	Midpoint (reference value) of the wind-generation uncertainty interval
$P^{\hat{W}T}$	Half-width of the wind-generation uncertainty interval
$P^{\tilde{P}V}$	Midpoint (reference value) of the PV-generation uncertainty interval
$P^{\hat{P}V}$	Half-width of the PV-generation uncertainty interval
$H^{\tilde{L}oad}$	Midpoint (reference value) of the thermal-demand uncertainty interval
$H^{\hat{L}oad}$	Half-width of the thermal-demand uncertainty interval
$POLY1$	Wind-generation uncertainty-margin variable
$POLY2$	PV-generation uncertainty-margin variable
$POLY3$	Electrical-demand uncertainty-margin variable
$POLY4$	Gas-demand uncertainty-margin variable
$POLY5$	Thermal-demand uncertainty-margin variable
EBS, EGS, EHS	Storage State of Charge
$\eta BS, \eta HS, \eta GS$	Efficiency of Energy Storage Systems (BES, Gas, Heat)
CBS, CGS, CHS	Capacity of Energy Storage Systems (BES, Gas, Heat)
PBS^C, PGS^C, PHS^C	Charge Power of Energy Storage Systems (BES, Gas, Heat)
PBS^d, PGS^d, PHS^d	Discharge Power of Energy Storage Systems (BES, Gas, Heat)
$Eload, Hload, Gload$	Final Load Value
$Eload^S, Hload^S, Gload^S$	Added Load in Demand Response Programs
$Eload^C, Hload^C, Gload^C$	Cut Load in Demand Response Programs
α^S / α^C	Permitted Load Change Percentage in Demand Response Programs
$PFuel-Cell$	Fuel Cell Output
$EH2(t)$	Hydrogen Stored in Tank
$EH2_{Treshold}$	Minimum Hydrogen Storage Required Until End of Time Horizon
$\eta Fuel-Cell$	Fuel Cell Efficiency (Hydrogen to Power Conversion)
$EH2_{\min}$	Minimum Allowed Hydrogen Level in Tank
$EH2_{\max}$	Maximum Allowed Hydrogen Level in Tank
$H2_S2G$	Hydrogen Consumption Rate by Fuel Cell
$\eta H2_P2G$	Electrolyzer Efficiency

$PH2_P2G(t)$	Input Power to Electrolyzer for Hydrogen Production
$EmissionG$	Emission Rate of Controllable Generators
$EmissionGT$	Gas Turbine Emission Rate
$EmissionGB$	Gas Boiler Emission Rate
$EmissionCHP$	CHP Units Emission Rate
$\underline{P^{Load}}, \overline{P^{Load}}$	Lower and upper admissible bounds of electrical demand
$\underline{G^{Load}}, \overline{G^{Load}}$	Lower and upper admissible bounds of gas demand
$\underline{P^{WT}}, \overline{P^{WT}}$	Lower and upper admissible bounds of wind-turbine generation
$\underline{P^{PV}}, \overline{P^{PV}}$	Lower and upper admissible bounds of PV generation
$\underline{H^{Load}}, \overline{H^{Load}}$	Lower and upper admissible bounds of thermal demand

1. Introduction

1.1. Background and Motivation

In recent decades, the energy landscape has undergone profound changes [1]. The increasing penetration of variable renewable resources, the expansion of digital and industrial loads, fossil fuel constraints, and the need for carbon emission reduction have made traditional single-carrier systems insufficient [2, 3]. Under these conditions, multi-carrier systems and particularly energy hubs have been introduced as comprehensive platforms for integrating, converting, and storing multiple carriers such as electricity, gas, heat, and hydrogen [4, 5]. These structures enable coordinated utilization of diverse resources and provide a foundation for building sustainable and future-oriented energy systems. Despite these advantages, the operation of energy hubs faces significant challenges. The stochastic nature of renewable generation and the variability of demand introduce high levels of uncertainty into planning [6]. At the same time, the requirement for operational flexibility and fast responsiveness highlights the importance of demand-side programs and storage technologies. Moreover, the deployment of Behind-the-Meter (BTM) assets such as PV and batteries, along with the expanding hydrogen chain, has further complicated the energy management landscape while also creating new opportunities [7]. Consequently, the development of frameworks that can manage the interactions among carriers, local resources, and demand in an integrated and uncertainty-resilient manner has become a strategic necessity for the design and operation of next-generation energy systems.

1.2. Literature Review

In [8], a multi-objective framework for integrated electricity–gas–heat networks are developed, combining renewables, Electric Vehicles (EVs), and hydrogen/thermal storage. Scenario-based robust optimization and fuzzy decision-making are applied to balance cost, losses, and reliability. The main novelty is the joint integration of advanced storage, waste-to-energy units, and market participation in a flexible hub model. In [9], a multi-carrier hub with a micro modular reactor, renewables, and storage is assessed for year-round electricity, heat, and cooling supply. Implemented in GAMS, the model employs demand response and Monte Carlo–based uncertainty handling. Innovation lies in coupling nuclear micro-reactors with renewables and trigeneration to reduce grid dependence and emissions. In [10], a hierarchical distributed framework for regional electricity–heat–gas systems are proposed, enhancing efficiency and low-carbon supply. Key novelties include carbon credit/green certificate trading, inter-layer coordination via cascading goals, and joint economic–environmental optimization. In [11], a two-stage multi-objective optimization framework is proposed for the efficient operation of multi-carrier energy systems under renewable uncertainty. The first stage minimizes operational costs using a scenario-based stochastic model, while the second enhances flexibility and reduces emissions by maximizing electrical and thermal generation capacities In [12], a stochastic tri-objective model for multi-carrier energy hub planning is developed to minimize cost, emissions, and consumer dissatisfaction. The framework integrates renewables, biomethane, hydrogen, and storage with demand response, applies an ε-constraint method to obtain the Pareto front, and uses fuzzy satisfaction for final solution selection. Its novelty lies in explicitly modeling consumer dissatisfaction within demand response, thus uniting economic, environmental, and social objectives. In [13], the authors present an optimal scheduling model for power-gas-heat energy hubs using simultaneous BTM and demand response programs. In this paper, uncertainties on the generation and demand sides are modeled and managed using box uncertainty sets. In [14], a MINLP model of three interconnected energy–water hubs are developed to jointly minimize operational costs, financial risks, and underground freshwater extraction. Stochastic optimization and the downside risk constraint method are employed to capture uncertainties, while TOPSIS prioritizes solutions. Results show that a small increase in operating cost can nearly eliminate well extraction and significantly reduce risk, highlighting both environmental and economic benefits. In [15], a multi-objective control strategy is proposed to improve the operation of integrated multi-energy hubs, targeting both economic efficiency and low-carbon performance. The model distributes electrical and thermal loads while ensuring frequency and pressure stability through a distributed control approach that requires only neighbor-to-neighbor information exchange. Its novelty lies in combining economic and environmental objectives within a low-communication, resilient framework for sustainable hub operation. In [16], a coordinated scheduling model for electricity–gas–heat integrated energy systems is developed to jointly enhance flexibility and reliability under renewable energy uncertainty. The framework derives flexibility demand and resource expressions, incorporates dynamic models of gas pipelines and heat flows, and introduces indices for flexibility, reliability, and their coordination. In [17], a MILP-based scheduling framework is proposed for a multi-energy hub integrating electricity, gas, and heat**,** supplemented by wind power, energy storage, and demand response programs. The hub comprises Combined Heat and Power (CHP) units, boilers, converters, and both thermal and electrical storage. The key novelty lies in coordinating multi-carrier energy flows with demand response flexibility, enabling load shifting, cost reduction, and greater renewable utilization. In [18], a hydrogen–electric–thermal tri-generation system is proposed, integrating PV power generation with a supercritical CO_2 Brayton cycle to fully utilize the solar spectrum. Three operating modes (Hydrogen–electricity–heat) are analyzed through thermodynamic modeling and optimization. In [19], a supply–demand optimization strategy for integrated energy systems is proposed, addressing renewable (wind and PV) uncertainties through a robust stochastic model and enhancing flexibility via a hybrid electricity–heat–hydrogen storage framework. On the demand side, an integrated demand response scheme is introduced to encourage user participation. In [20], a 24-h MILP model was developed for a residential PV prosumer to compare battery, Vehicle-to-Home (V2H), and hybrid battery–V2H configurations under clear and partly cloudy conditions. The study jointly evaluated operating cost, PV self-consumption, grid purchase, and power export under different PV–load deviation levels. Table 1 provides a feature-based comparison between selected recent studies and the present work.

Table 1. Comparison of modeling features in selected recent studies and the present work.

Ref	Energy carriers				Polyhedral uncertainty sets	BES degradation	Emission	BTM-PV-BES	Demand response implementation
	Electricity	Heat	Gas	Hydrogen					
[8]	✓	✓	✓	✓	✗	✗	✗	✗	✓
[9]	✓	✓	✗	✗	✗	✗	✓	✗	✓
[10]	✓	✓	✓	✗	✗	✗	✓	✗	✗
[11]	✓	✓	✓	✗	✗	✗	✓	✗	✓
[12]	✓	✓	✓	✓	✗	✗	✓	✗	✓
[13]	✓	✓	✓	✗	✗	✗	✗	✓	✓
[14]	✓	✓	✗	✗	✗	✗	✗	✗	✗
[15]	✓	✓	✗	✗	✗	✗	✓	✗	✗
[16]	✓	✓	✓	✗	✗	✗	✗	✗	✗
[17]	✓	✓	✓	✗	✗	✗	✗	✗	✓
[18]	✓	✓	✗	✓	✗	✗	✗	✗	✗
[19]	✓	✓	✗	✓	✗	✓	✗	✗	✓
[20]	✓	✗	✗	✗	✗	✗	✗	✓	✗
Current work	✓	✓	✓	✓	✓	✓	✓	✓	✓

1.3. Research Gaps and Contributions

Table 1 clarifies the methodological gap by comparing the combinations of modeling features considered in recent studies. Studies [8] and [12] coordinate electricity, gas, heat, and hydrogen together with demand-side flexibility; however, neither includes BTM PV–BES operation, polyhedral uncertainty sets, or degradation-aware battery operating constraints, and only [12] incorporates emission accounting. Study [13] combines BTM PV–battery operation and demand response within an electricity–gas–heat energy hub, but does not include hydrogen, polyhedral uncertainty sets, degradation-aware battery constraints, or emission accounting. Study [19] considers electricity, heat, and hydrogen together with demand response and degradation-aware energy storage, but does not represent the gas carrier, BTM PV–BES operation, polyhedral uncertainty sets, or emissions. Study [20] addresses BTM PV–battery operation at the residential level, but does not consider multi-carrier coupling, hydrogen, multi-carrier demand response, polyhedral uncertainty sets, degradation-aware battery constraints, or technology-specific emissions. The remaining studies summarized in Table 1 cover smaller subsets of these modeling features. Therefore, among the studies compared in Table 1, none incorporates the complete combination of four-carrier coordination, BTM PV–BES operation, multi-carrier demand response, polyhedral uncertainty treatment, degradation-aware battery operating constraints, and technology-specific emission accounting considered in the present framework.

The contribution of this work consequently does not rely on treating any of these elements as new in isolation. Instead, it lies in their operational coupling within the same scheduling problem. The BTM PV–BES system is explicitly connected to the hub-level electricity balance through distinct local-use, storage, grid-purchase, and export routes, while demand response redistributes electrical, gas, and thermal demands over the scheduling horizon. At the same time, uncertainty is represented for wind generation, PV generation, electrical demand, gas demand, and thermal demand and is embedded in the coupled electricity, gas, and heat balances. Battery operation is further constrained through intertemporal state-of-charge and charging/discharging variation limits intended to restrict aggressive cycling. This formulation makes it possible to examine how customer-side resources, demand-side flexibility, uncertainty, storage operation, and multi-carrier conversion interact rather than evaluating these features as separate additions to the energy hub.

Accordingly, the specific contributions of this study are summarized as follows:

- A unified electricity–gas–heat–hydrogen scheduling model is formulated in which hub-level conversion and storage resources are coordinated with BTM PV–BES power routing and demand response applied to electrical, gas, and thermal loads.
- The polyhedral uncertainty formulation represents deviations in both wind and PV generation together with electrical, gas, and thermal demands and incorporates these uncertainty terms directly into the coupled multi-carrier balance equations.
- Intertemporal state-of-charge and charging/discharging variation constraints are incorporated to restrict aggressive battery operation while preserving the scheduling flexibility of the BTM PV–BES system. These constraints represent degradation-aware operating limits rather than an explicit capacity-fade or state-of-health model.
- Technology-specific emissions are evaluated together with operating cost across four configurations defined under common system assumptions: the baseline system, BTM resources only, demand response only, and coordinated BTM–demand-response operation. This structure separates the individual and combined effects of the two flexibility mechanisms and reveals whether their economic and environmental effects move in the same direction.

The distinction of the proposed framework therefore arises from the interaction of these modeling layers within the same multi-carrier scheduling problem and from the controlled evaluation of their individual and coordinated effects. Table 1 positions this combination directly against the selected recent studies.

1.4. Paper Structure

The remainder of this paper is organized as follows:

Section 2, presents the mathematical modeling of the proposed multi-carrier energy hub, including the formulation of the objective function, operational constraints, and robust optimization framework. Section 3, discusses the numerical simulations and analyzes the results under different operational scenarios to evaluate the effectiveness of the proposed model. Section 4, concludes the paper by summarizing the main findings and outlining promising directions for future research.

2. Problem Formulation

Equation (1) represents the objective function of this study, which aims to minimize the total operational cost of a multi-carrier energy system. Its main components are summarized as follows:

$$
\begin{aligned}
Z = & \sum_t [CUP(t).PUP(t)] + \\
& \sum_t CGW(t).GGW(t) + \sum_t [CG(t).PG(t) + SUG(t) + SDG(t)] \\
& + \sum_t [CCHP(t).PCHP(t) + SUCHP(t) + SDCHP(t)] + \\
& \sum_t [Cself.(PPV2C(t) + PPV2ES(t) + PESS2C(t))] \\
& + \sum_t CG2C(t).PG2C(t)] + \\
& \sum_t [CG2ESS(t).(PG2ESS(t) - PESS2G(t))] - \\
& \sum_t CPV2G(t).PPV2G(t)]
\end{aligned} \tag{1}
$$

1. Electricity purchase cost from the main grid: Calculated based on hourly electricity prices and imported power, considering peak and off-peak tariffs.
2. Natural gas purchase cost: Used to supply gas-consuming units (e.g., CHP), subject to flow limits and time-varying gas prices.
3. Local generator operating cost: Includes electricity generation costs and start-up/shut-down costs of controllable local units.
4. CHP unit cost: Modeled for electricity generation only, accounting for operational and switching costs; the gas consumption maintains the coupling between electricity and heat.
5. Internal energy exchange cost: Covers solar power used locally, storage charging/discharging, and applies a uniform cost to enhance economic accuracy.
6. Load supply cost from networks: Represents the dependency of local loads on electricity and gas grids for cost evaluation.
7. Bidirectional exchange between storage and grid: Charging energy from the grid is a cost, while discharging to the grid is an income; modeled as a net term.
8. Revenue from solar power export: Entered with a negative sign, reducing total cost and reflecting economic gains from renewable energy sales.

Equations (2)–(7) define the operating limits and commitment logic of the local generator [21,22]. Equations (2) and (3) impose the minimum and maximum generation limits as functions of the binary commitment state, so the unit produces within its admissible range when online and remains off otherwise. Equations (4) and (5) represent start-up costs at the initial interval and subsequent OFF-to-ON transitions, respectively. Equations (6) and (7) apply the corresponding logic to shutdown costs, distinguishing the initial condition from later ON-to-OFF transitions. Together, these constraints couple generator dispatch with commitment changes and their associated switching costs over the scheduling horizon.

$$PG(t) \geq PG_{\min}.bv(t) \tag{2}$$

$$PG(t) \leq PG_{\max}.bv(t) \tag{3}$$

$$SUG(t) = CSU.bv(t) \tag{4}$$

$$SUG(t) = CSU.(bv(t) - bv(t-1) \tag{5}$$

$$SDG(t) = CSD.(-bv(t)) \tag{6}$$

$$SDG(t) = CSD.(-bv(t-1) - bv(t)) \tag{7}$$

Equations (8)–(18) describe the fuel-conversion characteristics, feasible operating region, and commitment behavior of the CHP unit [23–27]. Equations (8) and (9) couple gas consumption to electrical and thermal outputs through the corresponding conversion efficiencies. Equations (10) and (11) impose the admissible electrical and thermal output limits, respectively. The joint heat-and-power operating region is represented by Eqs. (12)–(14), which constrain the feasible combinations of electrical and thermal production while accounting for the CHP commitment state. Equations (15) and (16) represent start-up costs at the initial interval and during subsequent OFF-to-ON transitions, whereas Eqs. (17) and (18) describe the corresponding shutdown costs for the initial condition and later ON-to-OFF transitions. This formulation links fuel use, cogeneration outputs, feasible operating conditions, and intertemporal commitment decisions within the scheduling model.

$$PCHP(t) = \eta ECHP.GCHP(t) \tag{8}$$

$$HCHP(t) = \eta HCHP.GCHP(t) \tag{9}$$

$$PCHP_{\min} \leq PCHP(t) \leq PCHP_{\max} \tag{10}$$

$$HCHP_{\min} \leq HCHP(t) \leq HCHP_{\max} \tag{11}$$

$$\left[PCHP(t) - PCHP^A - \frac{PCHP^A - PCHP^B}{HCHP^A - HCHP^B}\left(HCHP - HCHP^A\right) \right] \leq 0 \tag{12}$$

$$\left[PCHP(t) - PCHP^B - \frac{PCHP^B - PCHP^C}{HCHP^B - HCHP^C}\left(HCHP - HCHP^B\right) \right] \geq -\left(1 - bvCHP(t)\right).\psi \tag{13}$$

$$\left[PCHP(t) - PCHP^C - \frac{PCHP^C - PCHP^D}{HCHP^C - HCHP^D}\left(HCHP - HCHP^C\right) \right] \geq -\left(1 - bvCHP(t)\right).\psi \tag{14}$$

$$SUCHP(t) \geq 0 \tag{15}$$

$$SUCHP(t) \geq SUCHP\left(bvCHP(t) - bvCHP(t-1)\right) \tag{16}$$

$$SDCHP(t) \geq 0 \tag{17}$$

$$SDCHP(t) \geq SDCHP(t)\left(bvCHP(t-1) - bvCHP(t)\right) \tag{18}$$

Equations (19)–(37) formulate the electrical, thermal, and gas storage systems in discrete time [12,28–33]. For the battery energy storage system, Eqs. (19) and (20) update the state of charge at the initial and subsequent intervals by accounting for charging and discharging power and storage efficiency. Equations (21) and (22) impose the minimum and maximum state-of-charge limits, while Eqs. (23) and (24) restrict the charging and discharging rates and enforce the corresponding operating mode. Equation (25) imposes the terminal state-of-charge requirement. Equations (26) and (27) further limit intertemporal state-of-charge variation and the difference between charging and discharging power, thereby restricting abrupt or aggressive battery operation without introducing an explicit capacity-fade or state-of-health model. The thermal-storage formulation in Eqs. (28)–(32) applies the same intertemporal principle to heat: the stored-energy balance is updated with charging and discharging flows, subject to storage-capacity, operating-mode, and terminal-reserve constraints. Equations (33)–(37) similarly describe gas-storage dynamics,

including gas injection and withdrawal efficiencies, admissible storage levels, mutually exclusive charging/discharging operation, and the required terminal gas inventory.

$$EBS(t=1)=\frac{\eta BS.PBS^{C}(1)}{CBS}-\frac{PBS^{d}(1)}{\eta BS.CBS} \quad (19)$$

$$EBS(t)=EBS(t-1)+\frac{\eta BS.PBS^{C}(t)}{CBS}-\frac{PBS^{d}(t)}{\eta BS.CBS} \quad (20)$$

$$EBS(t)\geq \underline{EBS} \quad (21)$$

$$EBS(t)\leq \overline{EBS} \quad (22)$$

$$PBS^{C}(t)\leq PBS^{C}.bvBS(t) \quad (23)$$

$$PBS^{d}(t)\leq \eta BS.\overline{PBS^{d}}.(1-bvBS(t)) \quad (24)$$

$$EBS(t)\geq EBS_Treshold \quad (25)$$

$$\left|EBS(t)-EBS(t-1)\right|\leq \overline{\Delta EBS} \quad (26)$$

$$\left|PBS^{C}(t)-PBS^{d}(t)\right|\leq \overline{PBS^{r}} \quad (27)$$

$$EHS(t)=EHS(t-1)+\frac{\eta HS.PHS^{C}(t)}{CHS}-\frac{PHS^{d}(t)}{\eta HS.CHS} \quad (28)$$

$$\underline{EHS}\leq EHS(t)\leq \overline{EHS} \quad (29)$$

$$0\leq PHS^{C}(t)\leq bvHS(t).PHS^{r} \quad (30)$$

$$0\leq PHS^{d}(t)\leq (1-bvHS(t)).\eta BS.PHS^{r} \quad (31)$$

$$EHS(t)\geq EHS_Treshold \quad (32)$$

$$EGS(t)=EGS(t-1)+\frac{\eta GS.PGS^{C}(t)}{CGS}-\frac{PGS^{d}(t)}{\eta GS.CGS} \quad (33)$$

$$\underline{EGS}\leq EGS(t)\leq \overline{EGS} \quad (34)$$

$$0\leq PGS^{C}(t)\leq bvGS(t).PGS^{r} \quad (35)$$

$$0\leq PGS^{d}(t)\leq (1-bvGS(t)).\eta GS.PGS^{r} \quad (36)$$

$$EGS(t)\geq EGS_Treshold \quad (37)$$

Equations (38)–(43) formulate the hydrogen production, storage, and electricity-reconversion chain [34]. Equation (38) defines the hydrogen inventory at the initial interval from electrolyzer production and hydrogen withdrawal, while Eq. (39) extends this balance to subsequent periods using the previous tank inventory. Equations (40) and (41) impose the minimum and maximum hydrogen-storage limits, and Eq. (42) enforces the terminal inventory requirement at the end of the scheduling horizon. Equation (43) converts hydrogen withdrawal into fuel-cell electrical output through the corresponding conversion efficiency. As illustrated in Figure 1, the electrolyzer is supplied electrically and produces hydrogen for storage, which can later be withdrawn for fuel-cell generation; no direct natural-gas input is used in this hydrogen-production route. Figure 1 is redrawn based on [35].

$$EH2(1)=\eta H2_P2G.PH2_P2G(1)-H2_S2G(1) \quad (38)$$

$$EH2(t)=EH2(t-1)+\eta H2_P2G.PH2_P2G(t)-H2_S2G(t) \quad (39)$$

$$EH2(t)\geq EH2_{\min} \quad (40)$$

$$EH2(t)\geq EH2_{\max} \quad (41)$$

$$EH2(t)\geq EH2_{Treshold} \quad (42)$$

$$PFuel-Cell=\eta Fuel-Cell.H2_S2G(t) \quad (43)$$

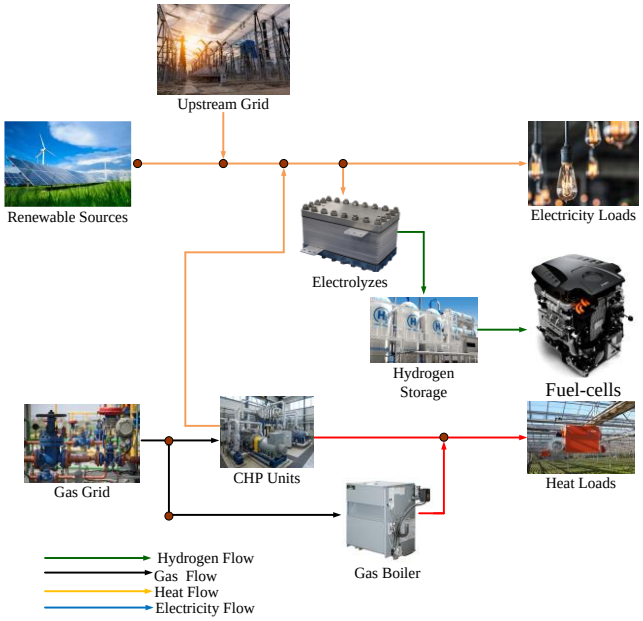

Fig. 1. Integrated hydrogen hub showing hydrogen production, storage, and utilization.

Equations (44)–(55) formulate demand response for electrical, gas, and thermal loads [36–39]. For electricity, Eq. (44) defines the scheduled demand as the reference load adjusted by upward and downward shifts, while Eq. (45) preserves energy neutrality by balancing the total upward and downward adjustments over the scheduling horizon. Equations (46) and (47) limit the allowable upward and downward electrical-demand changes relative to the reference load. The same structure is applied to gas demand in Eqs. (48)–(51): the adjusted gas load is formed from the reference profile, the total shifted amount is conserved, and the upward and downward variations are bounded. Equations (52)–(55) extend this formulation to thermal demand. Thus, the three demand-response models redistribute consumption across time while preserving the corresponding total demand over the scheduling horizon.

$$Eload=Eload(t)+Eload^{S}(t)-Eload^{C}(t) \quad (44)$$

$$\sum_{t=1}^{T} Eload^{S}(t) = \sum_{t=1}^{T} Eload^{C}(t) \quad (45)$$

$$0 \le Eload^{S}(t) \le \alpha^{S} Eload \quad (46)$$

$$0 \le Eload^{C}(t) \le \alpha^{C} Eload \quad (47)$$

$$Gload = Gload(t) + Gload^{S}(t) - Gload^{C}(t) \quad (48)$$

$$\sum_{t=1}^{T} Gload^{S}(t) = \sum_{t=1}^{T} Gload^{C}(t) \quad (49)$$

$$0 \le Gload^{S}(t) \le \alpha^{S} Eload \quad (50)$$

$$0 \le Gload^{C}(t) \le \alpha^{C} Gload \quad (51)$$

$$Hload = Hload(t) + Hload^{S}(t) - Hload^{C}(t) \quad (52)$$

$$\sum_{t=1}^{T} Hload^{S}(t) = \sum_{t=1}^{T} Hload^{C}(t) \quad (53)$$

$$0 \le Hload^{S}(t) \le \alpha^{S} Hload \quad (54)$$

$$0 \le Hload^{C}(t) \le \alpha^{C} Hload \quad (55)$$

Equations (56)–(58) describe the electric heat pump. Equation (56) relates electrical consumption to thermal output through the heat-pump conversion coefficient. Equation (57) imposes the admissible electrical operating range, while Eq. (58) limits the change in heat-pump electrical consumption between consecutive intervals. These constraints represent the heat pump as a controllable electricity-to-heat conversion unit within the coupled electricity and thermal balances.

$$HEHP(t) = \eta EHP.PEHP(t) \quad (56)$$

$$\underline{PEHP} \le PEHP(t) \le \overline{PEHP} \quad (57)$$

$$-\sigma EHP \le PEHP(t) - PEHP(t-1) \le \sigma EHP \quad (58)$$

Equations (59)–(61) formulate the electrically supplied thermal boiler [40]. Equation (59) couples electrical input to thermal output through the conversion efficiency. Equation (60) imposes the admissible electrical operating range, while Eq. (61) limits intertemporal changes in boiler power through the prescribed ramp-rate constraint. The boiler therefore provides an additional controllable electricity-to-heat conversion path in the multi-carrier hub.

$$HTB(t) = \eta TB.PTB(t) \quad (59)$$

$$\underline{PTB} \le PTB(t) \le \overline{PTB} \quad (60)$$

$$-\sigma TB \le PTB(t) - PTB(t-1) \le \sigma TB \quad (61)$$

Equations (62)–(64) describe the gas turbine. Equation (62) links gas consumption to electrical generation through the turbine efficiency and fuel heating value. Equation (63) restricts the electrical output to its admissible operating range, while Eq. (64) limits the change in turbine output between consecutive intervals. These constraints couple the gas and electricity carriers while retaining the turbine capacity and ramping requirements.

$$\rho GT(t) = \frac{PGT(t)}{\eta GT} \quad (62)$$

$$\underline{PGT} \le PGT(t) \le \overline{PGT} \quad (63)$$

$$-\sigma^{GT} \le PGT(t) - PGT(t-1) \le \sigma^{GT} \quad (64)$$

Equations (65)–(67) formulate the power-to-gas unit. Equation (65) relates electrical input to synthetic-gas production through the specified conversion efficiency and gas heating value. Equation (66) imposes the unit operating limits, and Eq. (67) restricts intertemporal changes in electrical input through the prescribed ramp-rate constraint. This conversion route enables electricity to be transferred to the gas carrier within the integrated hub.

$$GP2G(t) = \eta P2G.PP2G(t) \quad (65)$$

$$\underline{PP2G} \le PP2G(t) \le \overline{PP2G} \quad (66)$$

$$-\sigma P2G \le PP2G(t) - PP2G(t-1) \le \sigma P2G \quad (67)$$

Equations (68) and (69) describe the gas-fired boiler [41]. Equation (68) converts gas consumption into useful thermal output through the boiler efficiency, whereas Eq. (69) imposes the admissible gas-input or thermal-output operating range. The unit therefore couples the gas and heat balances of the energy hub.

$$HGB(t) = \eta GB.GGB(t) \quad (68)$$

$$\underline{GGB} \le GGB(t) \le \overline{GGB} \quad (69)$$

Equations (70)–(75) quantify the operational emissions represented in the model. Equation (70) calculates emissions from the local generator by applying its emission factor to electrical output, and Eq. (71) applies the corresponding factor to gas-turbine generation. Equation (72) evaluates gas-boiler emissions from fuel consumption, the higher heating value, and the technology-specific emission factor. Equation (73) uses the same fuel-based structure for the CHP unit, while Eq. (74) accounts for emissions associated with gas purchased from the upstream network. Equation (75) aggregates these technology-specific contributions over all scheduling intervals to obtain total system emissions. Within this accounting boundary, upstream emissions associated with purchased natural gas are included through Eq. (74), whereas imported electricity is not assigned a separate upstream emission factor. This convention is applied consistently to all four case studies so that the scenario comparison is performed on the same emission basis.

$$EmissionG(t) = \delta G.PG(t) \quad (70)$$

$$EmissionGT(t) = \delta GT.PGT(t) \quad (71)$$

$$EmissionGB(t) = \delta GB.(GGB(t).HHV) \quad (72)$$

$$EmissionCHP(t) = \delta CHP.(GCHP(t).HHV) \quad (73)$$

$$EmissionGW(t) = \delta GW.(GGW(t).HHV) \quad (74)$$

Equations (76)–(79) define the main electricity-routing paths of the BTM PV–battery configuration. Equation (76) allocates PV generation among direct supply to the local load, battery charging, and export to the grid. Equation (77) defines total battery charging as the combination of PV-to-storage and grid-to-storage power. Equation (78) decomposes battery discharge into power supplied to the local load and power exported to the grid. Finally, Eq. (79) imposes the local-load balance, in which demand can be supplied by direct PV

generation, battery discharge, and electricity purchased from the grid. These routing constraints explicitly distinguish local use, storage, and grid exchange within the BTM system.

$$TotalEmission = \sum_{t} \begin{bmatrix} EmissionG(t) + \\ EmissionGT(t) + \\ EmissionGB(t) + \\ EmissionCHP(t) + \\ EmissionGW(t) \end{bmatrix} \quad (75)$$

For scheduling purposes, the BTM PV–battery system is treated as a customer-side resource whose admissible power exchanges are coordinated by the central energy-hub scheduler. The formulation does not represent ownership transfer or bilateral contracts; instead, it assumes that the BTM power flows are visible to the scheduler within the routing limits defined by Eqs. (76)–(79). PV generation may supply the local load, charge the battery, or be exported to the grid; the battery may supply the local load or export electricity, while grid electricity may supply either the local load or battery charging. Economically, local PV and storage use are represented by the internal self-use term in the objective function, grid-to-load purchases are charged at the prescribed purchase cost, grid-to-storage charging and storage-to-grid discharge are represented through the net grid–storage exchange term, and PV export is credited at the specified selling price. The same assumptions are used in all BTM-enabled case studies.

$$PPV(t) = PPV^{C}(t) + PPV^{ES}(t) + PPV^{G}(t) \quad (76)$$

$$PES^{C}(t) = PPV^{ES}(t) + PG^{ES}(t) \quad (77)$$

$$PES^{d} = PES^{C}(t) + PES^{G}(t) \quad (78)$$

$$Eload = PPV^{C}(t) + PES^{C}(t) + PG^{C}(t) \quad (79)$$

Uncertainty is represented for five time-dependent quantities: wind generation, PV generation, electrical demand, gas demand, and thermal demand. For each quantity, an admissible interval of ±10% around its reference value is considered. Accordingly, Eqs. (80)–(84) define the corresponding upper and lower bounds, while Eqs. (85)–(94) calculate the midpoint and half-width of each interval. With symmetric ±10% bounds, the midpoint coincides with the reference value and the half-width represents a 10% deviation from that value. Equations (95)–(99) introduce the non-negative deviation variables associated with wind generation, PV generation, electrical demand, gas demand, and thermal demand, respectively. These variables are constrained by the corresponding half-widths and are subsequently embedded in the multi-carrier balance equations. The adopted formulation therefore represents unfavorable operating conditions by reducing available renewable generation and increasing energy demands relative to their reference values. In all four case studies reported in this work, the uncertainty scaling coefficient is fixed at (ξ =1), corresponding to the full prescribed ±10% deviation range.

$$\underline{P^{Load}} \le P^{Load} \le \overline{P^{Load}} \quad (80)$$

$$\underline{G^{Load}} \le G^{Load} \le \overline{G^{Load}} \quad (81)$$

$$\underline{P^{WT}} \le P^{WT} \le \overline{P^{WT}} \quad (82)$$

$$\underline{P^{PV}} \le P^{PV} \le \overline{P^{PV}} \quad (83)$$

$$\underline{H^{Load}} \le H^{Load} \le \overline{H^{Load}} \quad (84)$$

$$P^{Load} = \frac{1.1 * P^{Load} + 0.9 * P^{Load}}{2} \quad (85)$$

$$P^{Load} = \frac{1.1.P^{Load} - 0.9.P^{Load}}{2} \quad (86)$$

$$G^{Load} = \frac{1.1.G^{Load} + 0.9.G^{Load}}{2} \quad (87)$$

$$G^{Load} = \frac{1.1.G^{Load} - 0.9.G^{Load}}{2} \quad (88)$$

$$P^{WT} = \frac{1.1.P^{WT} + 0.9.P^{WT}}{2} \quad (89)$$

$$P^{WT} = \frac{1.1.P^{WT} - 0.9.P^{WT}}{2} \quad (90)$$

$$P^{PV} = \frac{1.1.P^{PV} + 0.9.P^{PV}}{2} \quad (91)$$

$$P^{PV} = \frac{1.1.P^{PV} - 0.9.P^{PV}}{2} \quad (92)$$

$$H^{Load} = \frac{1.1.H^{Load} + 0.9.H^{Load}}{2} \quad (93)$$

$$H^{Load} = \frac{1.1.H^{Load} - 0.9.H^{Load}}{2} \quad (94)$$

$$POLY1 \ge P^{WT} \quad (95)$$

$$POLY2 \ge P^{PV} \quad (96)$$

$$POLY3 \ge P^{Load} \quad (97)$$

$$POLY4 \ge G^{Load} \quad (98)$$

$$POLY5 \ge H^{Load} \quad (99)$$

The wind and solar input profiles are represented statistically to provide exogenous renewable-generation trajectories for the 24-h scheduling problem. Wind generation is derived from a Weibull-based representation, whereas solar availability is described using a Beta-based representation, consistent with the data source in [42]. Figure 2 illustrates the resulting wind and PV profiles used by the optimization model. This treatment separates renewable-profile generation from the multi-carrier scheduling equations and avoids introducing detailed aerodynamic or device-level PV conversion models into the operational optimization.

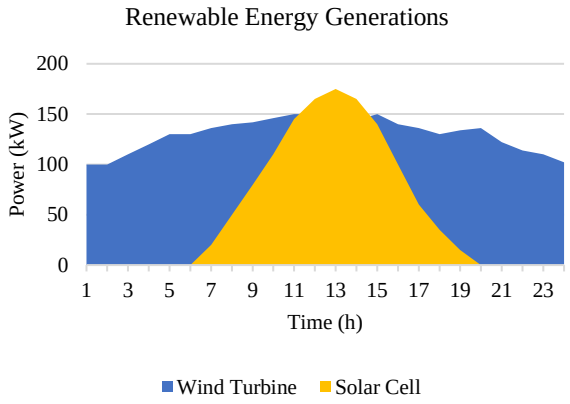

Fig. 2. Renewable energy modeling.

Equations (100)–(102) impose the robustified electricity, gas, and heat balances, respectively. Equation (100) coordinates electricity production, conversion, storage, grid exchange, hydrogen conversion, and electrical demand. Equations (101) and (102) impose the corresponding gas and thermal balances. Through the uncertainty terms defined in Eqs. (80)–(99), these balances are evaluated under reduced renewable availability and increased multi-carrier demand.

$$\begin{aligned}&(P^{WTT)+}(t)-\xi.Poly1)+(P^{PV}(t)-\xi.Poly2)\\&+PG(t)+PCH(t)+PBS^{d}+PUP(t)+PFC(t)=\\&PH2_P2G(t)+PEHP(t)+PBS^{c}(t)+PTB(t)\\&+(P^{Load}(t)+\xi.Poly3)\end{aligned} \tag{100}$$

$$\begin{aligned}&GP2G(t)+PGS^{d}(t)+GGW(t)\\&=\rho GT+GGB(t)+GCHP(t)+\\&PGS^{C}+(G^{Load}(t)+\xi.Poly4)\end{aligned} \tag{101}$$

$$\begin{aligned}&HGB(t)+HCHP(t)+HEHP(t)+\\&HTB(t)+PHS^{d}=\\&PGS^{C}+(H^{Load}(t)+\xi.Poly5)\end{aligned} \tag{102}$$

The optimization model is implemented in GAMS and solved as a mixed-integer linear program using CPLEX, with a relative optimality tolerance of 10^{-4}. Computational tractability is maintained by preserving a deterministic MILP structure: equipment relations and operating limits are expressed through linear constraints and binary status variables, while the robust uncertainty terms are embedded directly in the multi-carrier balance equations rather than expanded through scenario enumeration. Consequently, the 24-h case studies are solved directly with the CPLEX MIP solver without an additional decomposition procedure. Table 2 introduces the input data used in the modeling.

3. Simulation Results

This paper analyzes the performance of energy storage systems across four different case studies, each simulating specific conditions with various storage systems and constraints. The case studies are as follows:

1. Case Study 1 (CS1)**:** Evaluates the storage system without demand response programs or BTM systems, serving as a baseline.
2. Case Study 2 (CS2)**:** Examines the storage system with BTM systems but without demand response.
3. Case Study 3 (CS3)**:** Focuses on the storage system with demand response programs but without BTM systems.
4. Case Study 4 (CS4)**:** Analyzes the combination of both demand response programs and BTM.

These case studies highlight the effects of different configurations on energy storage performance and emphasize the importance of considering degradation constraints in real-world applications.

Table 2. Input data

Parameter	Value
Fuel Cell Efficiency	0.55
Electrolyzer Efficiency in Converting Electricity to Hydrogen	0.9
Maximum Power Generation Capacity of the CHP Unit	500 kW
Maximum Allowed Change Rate in Charge Status Between Two Time Intervals	0.05
Emission Factor per Unit of Electricity Produced by Generator	0.8
Emission Factor per Unit of Electricity Produced by Gas Turbine	0.5
Emission Factor per Unit of Electricity Produced by Gas Boiler	0.2
Emission Factor per Unit of Electricity Produced by CHP Unit	0.3
Emission Factor of Gas Received from the Network	0.1
Higher Heating Value of Gas	1
Maximum Allowed Difference Between Charge and Discharge in Each Time Interval	60 kW
Maximum Heat Generation Capacity of the CHP Unit	300 kW
Electrical Efficiency of CHP Unit	0.9
Thermal Efficiency of CHP Unit	0.95
Power-to-Gas Conversion Efficiency	0.9
Maximum Allowed Demand Increase Share from Nominal Load	15%
Maximum Allowed Demand Decrease Share from Nominal Load	5%
Ramp Rate of Power to Gas	50 kW
Maximum Thermal Boiler Consumption	500 kW
Maximum Thermal Boiler Output	300 kW
Ramp Rate of Thermal Boiler	50 kW
Start and Stop Cost of CHP Unit	0.3
Gas Boiler Efficiency	0.9
Electrical Storage Capacity	1000 kW
Storage Charge Status Threshold	50 kW
Gas Storage Capacity	800 kW
Gas Storage Efficiency	0.95
Thermal Storage Efficiency	0.9
Electrical Storage Efficiency	0.95
Nominal Capacity of Thermal Storage	250 kWh
Maximum Power Generation Capacity of Thermal Generator	400 kW
Maximum Pump Output	200 kW
Maximum Charge and Discharge Rate of Thermal Storage	250 kW
Start and Stop Cost of Local Generators	0.5
Maximum Hydrogen Storage in Tank	500 kg
Maximum Power Exchange with Upstream Grid	1000
Maximum Gas Exchange with Upstream Grid	1500

Figure 3 compares the operating costs of the four configurations. CS1, without BTM resources or demand response, has the highest cost

at $14,528 and therefore serves as the reference case. Introducing BTM resources in CS2 reduces the cost to $11,281, corresponding to a 22.35% reduction. This result indicates that local PV generation and storage can reduce the use of higher-cost external electricity and improve temporal coordination between local generation and consumption. Demand response alone in CS3 reduces the cost more moderately to $13,661, or 5.97% below CS1, showing that load shifting provides economic flexibility but cannot substitute for local generation and storage. When BTM resources and multi-carrier demand response are coordinated in CS4, the cost decreases to $9,650, corresponding to a 33.58% reduction relative to CS1. The comparison therefore indicates that the main economic benefit arises from the complementary operation of local energy resources and demand-side flexibility rather than from either mechanism considered independently.

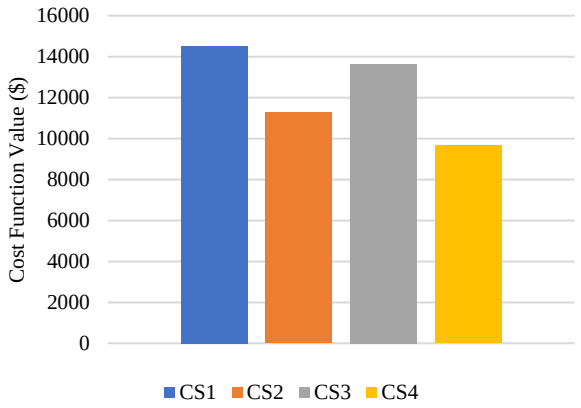

Fig. 3. Comparison of the objective function value in 4 case studies.

Figure 4 compares the total emissions obtained for the four configurations. CS1 produces 14,805.423 kg CO_2e and is used as the environmental reference. The inclusion of BTM resources in CS2 reduces emissions to 14,114.848 kg CO_2e, corresponding to a 4.66% reduction, because part of the energy requirement can be supplied through locally available resources and storage. In contrast, CS3 increases emissions to 15,382.616 kg CO_2e, approximately 3.90% above CS1, despite its lower operating cost. This result shows that cost-oriented demand shifting does not necessarily produce an emission reduction because the temporal redistribution of demand can modify the utilization of emission-producing units. In CS4, coordinating BTM resources with demand response limits emissions to 14,238.640 kg CO_2e, which is 3.83% below CS1. Importantly, CS2 achieves the lowest emissions, whereas CS4 achieves the lowest operating cost. The results therefore indicate a trade-off between the economic and environmental effects of the available flexibility mechanisms.

Figure 5 compares the electrolyzer power consumption across the four case studies. The operating schedule changes among the configurations because the electrolyzer competes with other electrical loads, storage units, and conversion technologies for the available electricity. In CS1 and CS2, electrolyzer operation is concentrated in fewer periods, whereas the introduction of demand response in CS3 and its coordination with BTM resources in CS4 modifies the timing of electricity allocation to hydrogen production. These differences illustrate the coupling between hydrogen production and the electricity-side scheduling decisions. Therefore, the electrolyzer should be interpreted as a flexible conversion unit whose operating pattern is determined jointly by electricity availability, system demand, and the economic objective rather than as an independently dispatched hydrogen source.

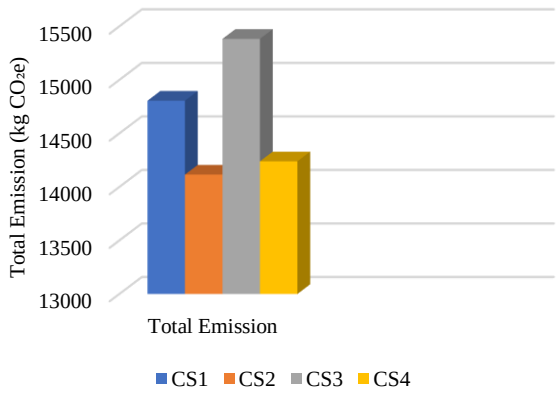

Fig. 4. Comparison of the total emission value in 4 case studies.

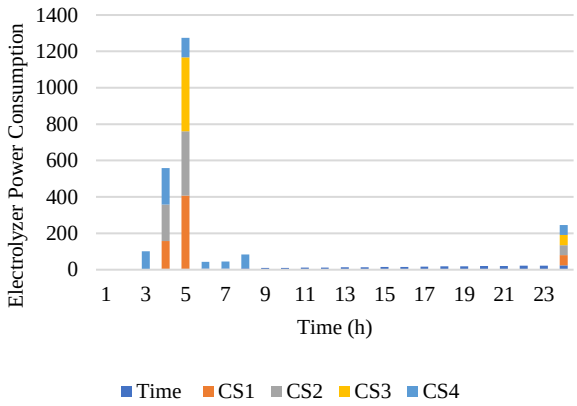

Fig. 5. Power consumption by electrolyzer.

Figure 6 shows the 24-h hydrogen inventory for the four case studies. In all configurations, hydrogen is produced during selected periods through the electrolyzer and stored for subsequent use by the fuel cell. The inventory trajectories differ among the cases because changes in BTM availability and demand-response operation modify the timing of electricity allocated to hydrogen production. The stored hydrogen is subsequently reduced when the fuel cell is activated, demonstrating the temporal coupling between the electrolyzer, hydrogen storage, and electricity supply. Despite differences in the intermediate trajectories, all configurations satisfy the prescribed terminal hydrogen-storage requirement. This behavior indicates that the hydrogen subsystem primarily provides intertemporal energy conversion and storage while remaining subject to the same final inventory condition in all four cases.

Figure 7 presents the fuel-cell power output for the four case studies. In all configurations, the fuel cell is activated at hour 20 and supplies 275 kW, while its output remains zero during the other periods. The identical dispatch across the four cases indicates that the introduction of BTM resources and demand response does not alter the optimal timing of fuel-cell utilization under the adopted parameters. Instead, these mechanisms mainly affect the upstream scheduling of electricity, storage, and hydrogen production. The result also shows that the stored hydrogen is retained until the period in which fuel-cell conversion becomes economically preferable within the optimized schedule.

Table 3**,** the analysis of buying and selling electricity across these different cases helps identify the operational efficiency, cost reduction potential, and optimal use of renewable resources for grid stability. In this analysis, four case studies are examined to evaluate electricity

trading with the grid under different operational conditions. **CS1** refers to normal operation without BTM systems, but includes wind turbines, solar panels, and various energy storage systems. In this case, no electricity is sold to the grid, and electricity is purchased from the grid to meet demand. **CS2** includes only BTM systems, where solar panels and storage batteries are integrated, and surplus electricity is sold to the grid, while electricity is purchased from the grid when needed. **CS3** involves demand response programs for electricity, gas, and heating, where consumption is actively managed during peak demand hours. As a result, the need to purchase additional electricity from the grid during sensitive hours is reduced compared to **CS1**. **CS4** combines BTM systems and demand response programs, where electricity generated from solar panels and batteries is sold to the grid, and demand response programs help reduce the purchase of electricity from the grid.

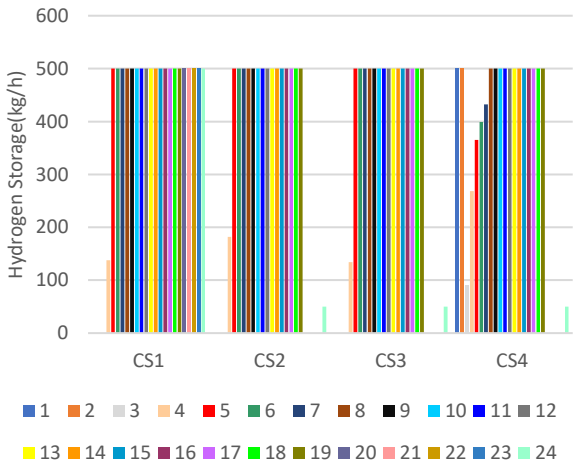

Fig. 6. Amount of hydrogen stored in the tank.

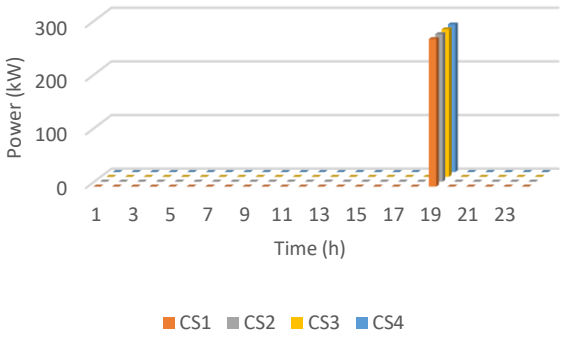

Fig. 7. Fuel cell power output in 4 case studies.

Table 4 summarizes the hourly gas exchange with the upstream gas network. No gas export occurs in any of the four configurations, indicating that the gas network acts exclusively as an external supply source under the adopted operating conditions. However, the amount of purchased gas changes considerably among the cases because demand response, CHP operation, gas-consuming conversion units, and storage decisions alter the internal gas balance. CS3 records the highest total gas purchase at 31,291.84, whereas CS4 has the lowest value at 25,751.49. This reduction in CS4 indicates that coordinating BTM resources with multi-carrier demand response affects not only electricity-side operation but also the coupled gas balance through changes in conversion-unit dispatch and carrier substitution. The gas results therefore provide additional evidence that the benefits of coordinated flexibility propagate across the interconnected energy carriers.

Table 3. Buying/selling electricity from the power grid in case studies.

Time	CS1	CS1	CS2	CS2	CS3	CS3	CS4	CS4
	Buy	Sell	Buy	Sell	Buy	Sell	Buy	Sell
1	779.505	–	658.889	–	620.047	–	961.739	–
2	852.136	–	725.96	–	814.421	–	946.704	–
3	858.579	–	847.778	–	874.421	–	1000.0	–
4	1000.0	–	1000.0	–	1000.0	–	1000.0	–
5	1000.0	–	1000.0	–	1000.0	–	1000.0	–
6	1000.0	–	1000.0	–	1000.0	–	1000.0	–
7	933.286	–	868.493	–	1000.0	–	1000.0	–
8	631.025	–	–	–	581.877	–	957.709	–
9	371.248	–	–	193.802	441.172	–	510.813	–
10	283.094	–	–	333.406	127.209	–	164.371	–
11	284.094	–	–	383.406	132.259	–	–	35.629
12	221.462	–	–	420.775	72.327	–	–	222.998
13	279.462	–	–	378.038	74.577	–	–	338.261
14	208.962	–	–	454.538	2.772	–	–	505.761
15	306.962	–	–	355.538	104.327	–	–	485.761
16	448.843	–	–	133.657	203.94	–	–	355.761
17	584.037	–	57.537	–	281.54	–	–	175.761
18	585.037	–	107.537	–	392.839	–	24.239	–
19	721.037	–	247.537	–	586.489	–	214.239	–
20	475.739	–	9.239	–	376.739	–	9.239	–
21	670.962	–	260.462	–	529.889	–	224.239	–
22	548.962	–	170.462	–	349.789	–	84.239	–
23	452.962	–	90.462	–	248.993	–	–	45.761
24	509.281	–	133.518	–	296.608	–	–	2.705

Table 4. Buying/selling gas from the gas grid in case studies.

Time	CS1	CS1	CS2	CS2	CS3	CS3	CS4	CS4
	Buy	Sell	Buy	Sell	Buy	Sell	Buy	Sell
1	830.538	–	689.737	–	771.638	–	1500.0	–
2	719.222	–	586.756	–	732.085	–	1500.0	–
3	706.388	–	465.924	–	759.188	–	1500.0	–
4	1034.347	–	885.368	–	1142.943	–	1500.0	–
5	1233.792	–	940.368	–	1339.09	–	1500.0	–
6	1231.57	–	1005.368	–	1311.838	–	1500.0	–
7	908.875	–	912.474	–	987.855	–	1500.0	–
8	874.748	–	984.195	–	1079.673	–	1500.0	–
9	1093.623	–	1093.623	–	1198.479	–	1500.0	–
10	1285.556	–	1285.556	–	1258.411	–	1500.0	–
11	1371.111	–	1371.111	–	1302.967	–	1500.0	–
12	1500	–	1500	–	1435.156	–	1500.0	–
13	1500	–	1500	–	1500	–	602.383	–
14	1500	–	1500	–	1500	–	623.316	–
15	1500	–	1500	–	1500	–	678.871	–
16	1500	–	1500	–	1500	–	734.427	–
17	1500	–	1500	–	1500	–	734.427	–
18	1500	–	1500	–	1500	–	734.427	–
19	1500	–	1500	–	1500	–	496.927	–
20	1500	–	1500	–	1500	–	496.927	–
21	1500	–	1500	–	1500	–	496.927	–
22	1500	–	1500	–	1500	–	686.927	–
23	1500	–	1500	–	1500	–	734.427	–
24	1474.36	–	1474.36	–	1472.513	–	731.503	–

Table 5. Sensitivity of CS4 to simultaneous adverse deviations in renewable generation and multi-carrier demands.

Deviation [%]	Cost [$]	Cost change [%]	Emissions [kg CO_2e]	Emission change [%]	Grid purchase	Grid export	Net grid exchange	Gas purchase
0.0	8,352.467	–	14,089.957	–	4,895.607	8,079.275	-3,183.668	27,675.343
2.5	8,881.660	6.336	14,189.327	0.705	4,974.324	6,986.654	-2,012.330	28,215.308
5.0	9,412.243	12.688	14,511.449	2.991	5,298.236	6,214.856	-916.619	28,677.206
7.5	9,946.285	19.082	14,575.945	3.449	5,505.145	5,212.837	292.308	29,203.320
10.0	10,482.263	25.499	14,723.804	4.499	5,613.882	4,075.105	1,538.776	29,442.738

Figure 8 compares the CHP operating profiles across the four case studies. The differences among the profiles reflect the coupled nature of CHP dispatch, since its operation simultaneously affects both the electricity and heat balances and is also linked to gas consumption. The inclusion of BTM resources changes the residual electrical demand that must be supplied by centralized conversion units, while demand response modifies the temporal distribution of electricity and heat requirements. Consequently, CHP operation varies across the four configurations as the optimizer reallocates energy among local generation, grid exchange, storage, and other conversion technologies. These results show that the effect of BTM resources and demand response on CHP operation should be interpreted through their influence on the coupled multi-carrier balance rather than solely through changes in CHP output magnitude.

Figure 9 compares the average charging and discharging behavior of the electrical, gas, and thermal storage systems across the four case studies. For the electrical storage system, CS2 exhibits the highest average charging and discharging levels, with average values of 45.50 and 47.57, respectively. In contrast, CS1, CS3, and CS4 show lower and relatively similar average values. This behavior indicates that the BTM configuration in CS2 relies more strongly on the battery for temporal redistribution of locally available electricity. When demand response is introduced, part of the temporal balancing requirement can instead be accommodated through load shifting, which reduces the need for the battery to provide the same level of energy shifting. The imposed limits on state-of-charge variation and charging/discharging power also restrict abrupt changes in battery operation and prevent unrestricted cycling within the scheduling horizon.

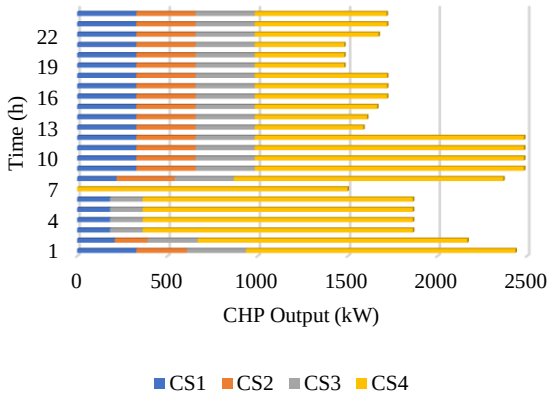

Fig. 8. CHP unit outputs in 4 case studies.

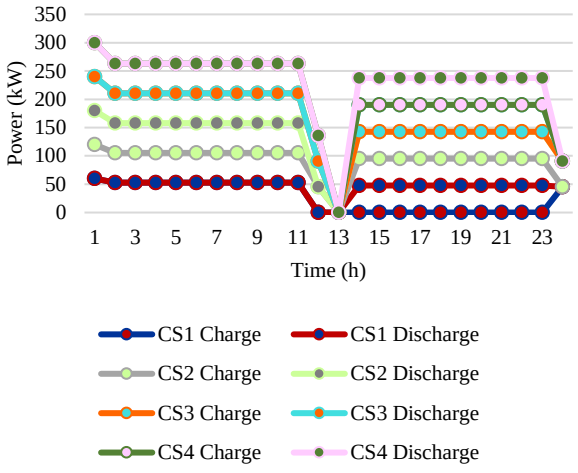

(a)

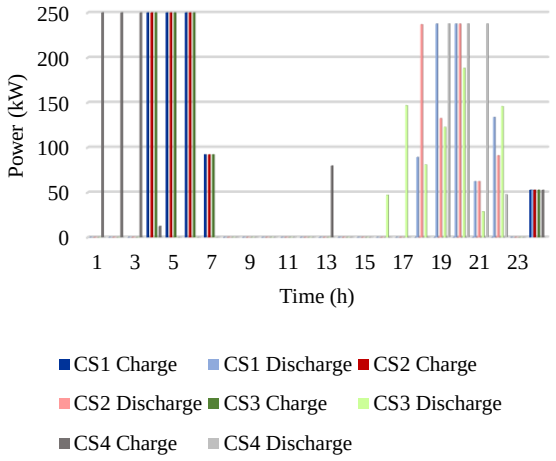

(b)

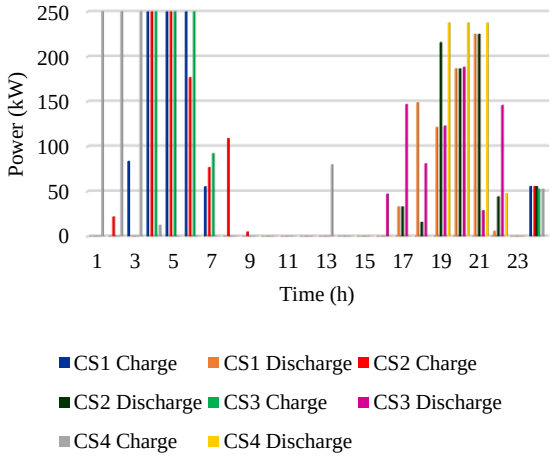

(c)

Fig. 9. Charge and discharge status: (a). Electrical storage. (b). Gas storage. (c). Heat storage.

For the gas storage system, the average charging level remains nearly unchanged across the four case studies, with an average value of 37.28. This suggests that the charging requirement is comparatively insensitive to the introduction of BTM resources and demand response under the adopted system conditions. The discharge behavior, however, varies among the cases. CS1 exhibits the highest average discharge value of 33.86, whereas CS2, CS3, and CS4 show lower values of approximately 31.67. The reduction in discharge indicates that the additional flexibility provided by BTM resources and/or demand response changes the balance between direct gas-network supply, storage utilization, and gas-consuming conversion units. Therefore, the main effect on gas storage is observed on the discharge side rather than on the charging side.

The thermal storage results show a similar dependence on system configuration. The average charging value is 39.35 in CS1 and CS2 and decreases to 37.28 in CS3 and CS4, indicating that the introduction of demand response modifies the temporal requirement for thermal-energy storage. For discharge, CS2 reaches the highest average value of 32.31, while CS3 and CS4 remain close to 31.67. These differences indicate that thermal storage and thermal demand response provide partly overlapping sources of flexibility: when thermal demand can be shifted, part of the temporal balancing requirement can be handled directly on the demand side rather than through additional storage cycling. Overall, Figure 9 shows that the three storage technologies respond differently to BTM and demand-response availability because each storage unit interacts with a different carrier balance and set of conversion technologies.

To evaluate the response of the integrated configuration to progressively less favorable operating conditions, an auxiliary sensitivity analysis is performed using the CS4 system structure. All technical capacities, economic parameters, storage characteristics, demand-response limits, and BTM settings are kept unchanged. Wind and PV availability are simultaneously reduced, while electrical, gas, and thermal demands are increased by 0%, 2.5%, 5%, 7.5%, and 10% relative to their nominal profiles. The resulting economic, emission, and grid-exchange responses are summarized in Table 5. This analysis is complementary to the four primary case studies and is used only to examine the effect of increasing adverse input deviations. As shown in Table 5, increasing the adverse deviation produces a clear deterioration in economic performance. Relative to the zero-deviation condition, the operating cost increases by 6.34%, 12.69%, 19.08%, and 25.50% at deviation levels of 2.5%, 5%, 7.5%, and 10%, respectively. At the 10% level, grid electricity purchase increases by 14.67% and gas purchase increases by 6.39%, while grid electricity export decreases from 8,079.275 to 4,075.105, corresponding to a 49.56% reduction. These changes indicate that renewable shortfalls combined with higher multi-carrier demands increase dependence on external energy supply.

Table 5 also shows a change in the direction of net electricity exchange. The system remains a net exporter at deviation levels of 0%, 2.5%, and 5%, with net exchanges of -3,183.668, -2,012.330, and -916.619, respectively, but becomes a net importer at 7.5% and 10%, reaching 292.308 and 1,538.776. Emissions increase more gradually than operating cost, reaching 14,723.804 kg CO_2e at the 10% level, which is 4.50% above the zero-deviation condition. Hydrogen production and fuel-cell utilization remain unchanged across the examined levels, suggesting that, under the adopted capacities and terminal hydrogen requirement, the hydrogen subsystem is less responsive to these adverse deviations than grid and gas exchanges.

4. Conclusion

This paper develops a robust scheduling framework for an integrated electricity–gas–heat–hydrogen energy hub with BTM PV–battery resources and multi-carrier demand response. Under the adopted system conditions, the operating cost decreases from $14,528 in CS1 to $11,281 in CS2, $13,661 in CS3, and $9,650 in CS4. Accordingly, demand response alone reduces the operating cost by 5.97% relative to CS1 rather than increasing it, while emissions rise by 3.90% from 14,805 to 15,383 kg CO_2e. BTM resources alone provide the lowest emissions, 14,115 kg CO_2e (4.66% below CS1), whereas the

coordinated BTM–demand-response configuration achieves the lowest operating cost with emissions of 14,239 kg CO_2e (3.83% below CS1). These results show that the minimum-cost and minimum-emission configurations do not coincide because cost-oriented demand shifting can modify the dispatch of emission-producing units even when the total operating cost decreases.

Overall, BTM resources provide the stronger emission benefit in the examined cases, whereas their coordination with demand response provides the strongest economic benefit. The preferred operating configuration therefore depends on the relative importance assigned to operating cost and emissions.

References

[1] V. Vijayan, "The Changing Energy Landscape", *Agricultural Engineering Today*, vol. 49, pp. 45-46, 2025.

[2] M. M. Amiri and M. Shafie-khah, "Investigation and feasibility of artificial intelligence in decarbonization of integrated gas and electricity network", in *Flexibility-Oriented Operation of Integrated Power and Gas Networks and Low-Carbon Technologies Under Clean Energy Transition*, pp. 193-230, 2026.

[3] A. Meydani, H. Shahinzadeh, G. B. Gharehpetian, M. M. Hayati, and M. Abapour, "Exploring the Role of Power-to-X in Energy Hubs", in *Power-to-X in Regional Energy Systems*, pp. 129-183, 2025.

[4] C. Gao, H. Lu, M. Chen, X. Chang, and C. Zheng, "A low-carbon optimization of integrated energy system dispatch under multi-system coupling of electricity-heat-gas-hydrogen based on stepwise carbon trading", *International Journal of Hydrogen Energy*, vol. 97, pp. 362-376, 2025.

[5] A. Ragab, M. Ebeed, A. Refai, A. M. Kassem, A. Ali, and H. H. Amin, "Energy Management of a Smart Multi-Carrier Energy Hub Systems for Low Carbon Emissions with a Carbon Capture Unit", *Sustainability*, vol. 18, pp. 6975, 2026.

[6] A. Safari, K. T. Tavana, M. T. Hagh, and A. E. Nezhad, "A Two-Stage Spatio-Temporal Flexibility-Based Energy Optimization of Internet Data Centers in Active Distribution Networks Based on Robust Control and Transformer Machine Learning Strategy", *Sustainable Computing: Informatics and Systems*, pp. 101214, 2025.

[7] Y. Manoharan, K. Olson, and A. J. Headley, "Sensitivity of energy storage system optimization program to the source of renewable energy in the presence of demand side management: A behind-the-meter case study", *Applied Energy*, vol. 388, pp. 125557, 2025.

[8] S. Parhoudeh, P. E. López, and A. K. Fard, "Multi-objective stochastic–adaptive robust optimization for energy management of grid-connected energy hubs including hydrogen and thermal storages, DGs and EVs, considering energy and reserve regulation market model", *Journal of Energy Storage*, vol. 135, pp. 118422, 2025.

[9] M. Moazen and M. Saghafi, "Performance optimization of an energy hub in the presence of a micro modular reactor and renewable energy sources", *Nuclear Engineering and Design*, vol. 444, pp. 114426, 2025.

[10] J. Yang, L. Lei, D. Liu, and W. Luo, "A distributed dispatch approach for district-level electric-heat-gas integrated energy systems considering carbon emission and green certificate trading", *Electric Power Systems Research*, vol. 244, pp. 111541, 2025.

[11] A. Garg, K. Niazi, S. Tiwari, S. Sharma, and T. Rawat, "Optimal energy management of multi-carrier energy system considering uncertainty in renewable generation", *Scientific Reports*, vol. 15, pp. 25936, 2025.

[12] A. Darvishi, B. Ranjbar, R. Gharibi, R. Khalili, and R. Dashti, "Multi-objective optimization of a socio-economic energy hub with demand response program and considering customer satisfaction", *Journal of Energy Storage*, vol. 100, pp. 113624, 2024.

[13] K. Taghizad-Tavana, M. Ghanbari-Ghalehjoughi, H. Niazi, M. T. Hagh, and A. E. Nezhad, "Robust operation of electricity–gas–heat energy hubs with behind-the-meter PV–battery and integrated demand response under uncertainty", *Energy Conversion and Management: X*, vol. 30, pp. 101505, 2026.

[14] S. Nojavan and H. Khoudeh, "Risk-based energy management of thermal-water-electricity nexus hubs via downside risk constraint technique", *Energy Reports*, vol. 13, pp. 1705-1727, 2025.

[15] S. Zhong, X. Wang, H. Wu, Y. He, B. Xu, and M. Ding, "Energy hub management for integrated energy systems: A multi-objective optimization control strategy based on distributed output and energy conversion characteristics", *Energy*, vol. 306, pp. 132526, 2024.

[16] Y. Zhang, J. Li, X. Ji, M. Yang, and P. Ye, "Optimal scheduling of electricity-gas-heat integrated energy system with coordination of flexibility and reliability", *Sustainable Energy Technologies and Assessments*, vol. 71, pp. 103968, 2024.

[17] R. H. Zubo, P. S. Onen, I. M. Mujtaba, G. Mokryani, and R. Abd-Alhameed, "Optimal Scheduling of a Multi-Energy Hub with Integrated Demand Response Programs", *Processes*, vol. 13, pp. 2879, 2025.

[18] X. Huang et al., "Thermodynamic analysis and optimization of a novel green hydrogen-electricity-heat tri-generation system based on full spectrum utilization of solar energy", *Energy Conversion and Management*, vol. 327, pp. 119527, 2025.

[19] S. Shi, Q. Gao, Y. Ji, J. Liu, H. Chen, and Y. Jiang, "A supply–demand optimization strategy for integrated energy system considering integrated demand response and electricity–heat–hydrogen hybrid energy storage", *Sustainable Energy, Grids and Networks*, vol. 42, pp. 101658, 2025.

[20] K. Taghizad-Tavana et al., "Comparative Residential Energy Management with Behind-the-Meter Battery and Vehicle-to-Home Operation Under Prescribed PV and Demand Deviations", *Energy Storage and Applications*, vol. 3, pp. 10, 2026.

[21] K. Taghizad-Tavana, H. S. Kheljani, S. H. Hosseini, M. Tarafdar-Hagh, and M. Daneshvar, "Multi-dimensional management of smart distribution networks: Comparative analysis of box and polyhedral methods for modeling uncertainties", *Sustainable Cities and Society*, vol. 108, pp. 105488, 2024.

[22] L. Huang, A. M. Mohsen, H. A. Kenjrawy, M. H. Almaamori, J. Zhang, and H. Rahbarimagham, "Robust Resilient Operation of the Renewable Energy Based Two-Way Electricity Distribution Network in the Presence of Energy Storage and Demand Response Programs", *International Journal of Energy Research*, vol. 2025, pp. 2067840, 2025.

[23] G. Zhang, Y. Ge, Z. Ye, and M. Al-Bahrani, "Multi-objective planning of energy hub on economic aspects and resources with heat and power sources, energizable, electric vehicle and hydrogen storage system due to uncertainties and demand response", *Journal of Energy Storage*, vol. 57, pp. 106160, 2023.

[24] S. Norouzi, M. Dadashi, S. Haghifam, H. Laaksonen, and K. Zare, "Offering strategy of price-maker energy hubs in integrated local electricity and heat markets", *Renewable Energy Focus*, vol. 53, pp. 100689, 2025.

[25] A. Dalimi-Asl, S. Javadi, A. Ahmarinejad, and P. Rabbanifar, "Optimal stochastic-probability management of resources and energy storage in energy hub considering demand response programs and uncertainties", *Sustainable Cities and Society*, vol. 99, pp. 104886, 2023.

[26] W. Hou, "Bi-level energy sharing model between multi-energy cloud energy storage and multiple integrated energy systems", *Electric Power Systems Research*, vol. 253, pp. 112541, 2026.
[27] A. Hamedi, A. R. Seifi, A. R. Abbasi, and D. Keihan Asl, "Optimizing CHP-based multi-carrier energy networks with advanced energy storage solutions", *Scientific Reports*, vol. 15, pp. 40874, 2025.
[28] Y. Pezhmani and N. Rezaei, "Risk-averse energy management of a water-heat-power virtual energy hub considering hosting capacity and Volt-VAR control of distribution network", *Energy*, vol. 318, pp. 134949, 2025.
[29] M. Sadeghian-Jahromi, M. Fotuhi-Firuzabad, S. Fattaheian-Dehkordi, F. Wang, and M. Lehtonen, "Simultaneous planning of distribution automation and battery energy storage systems for improving resilience of distribution network", *Sustainable Energy, Grids and Networks*, vol. 42, pp. 101709, 2025.
[30] F. Wang, W. Zheng, J. Zhao, and H. Forghan, "Enhancing efficiency and reliability of multi-energy systems: A hybrid heuristic algorithm for interconnected energy hubs", *Electric Power Systems Research*, vol. 231, pp. 110273, 2024.
[31] Y. Cao, J. Lei, and Z. Liu, "Multi-layered optimal scheduling method for multi-park energy systems based on price-based demand response uncertainty", *Electric Power Systems Research*, vol. 250, pp. 112149, 2026.
[32] S. S. Gougheri, H. Jahangir, M. A. Golkar, A. Ahmadian, and M. A. Golkar, "Optimal participation of a virtual power plant in electricity market considering renewable energy: A deep learning-based approach", *Sustainable Energy, Grids and Networks*, vol. 26, pp. 100448, 2021.
[33] J. Li et al., "Capacity optimization of rural residential distributed photovoltaic-Battery energy storage system considering uncertainties", *Journal of Energy Storage*, vol. 148, pp. 120246, 2026.
[34] H. Niazi, K. Taghizad-Tavana, A. Esmaeel Nezhad, A. Canani, M. Tarafdar Hagh, and P. Paidar, "Green Hydrogen in Integrated Multi-Energy Systems: Technological Pathways, Policy and Market Perspectives, and the Role of Artificial Intelligence", *Fuels*, vol. 7, pp. 37, 2026.
[35] K. Taghizad-Tavana, M. Ghanbari-Ghalehjoughi, A. Safari, M. T. Hagh, and A. E. Nezhad, "From green hydrogen production to artificial intelligence–driven energy management in hydrogen fuel cell electric vehicles: a comprehensive review of technologies, optimization techniques, international standards, and investment programs", *Applied Energy*, vol. 399, pp. 126534, 2025.
[36] E. Valipour, A. Babapour-Azar, R. Nourollahi, R. Khanjani-Shiraz, and M. Römer, "Risk-driven optimal scheduling of renewable-oriented energy hub under demand response program and energy storages: A novel Entropic value-at-risk modeling", *Sustainable Cities and Society*, vol. 107, pp. 105448, 2024.
[37] R. Bahmani, H. Karimi, and S. Jadid, "Stochastic electricity market model in networked microgrids considering demand response programs and renewable energy sources", *International Journal of Electrical Power & Energy Systems*, vol. 117, pp. 105606, 2020.
[38] M. Liu, X. Zhang, Y. Zhao, Y. Rong, S. Chen, and X. Gao, "Optimal scheduling of an integrated electricity-hydrogen-heat energy system considering electrolyzer flexibility and demand response", *International Journal of Hydrogen Energy*, vol. 202, pp. 152845, 2026.
[39] S. A. Mansouri, A. Ahmarinejad, M. S. Javadi, and J. P. Catalão, "Two-stage stochastic framework for energy hubs planning considering demand response programs", *Energy*, vol. 206, pp. 118124, 2020.
[40] P. Ren, Y. Dong, H. Zhang, C. Wang, J. Wang, and X. Fan, "Industrial hydrogen demand response for adaptive robust operation of electric hydrogen integrated energy systems", *Energy*, pp. 140353, 2026.
[41] H. Wang et al., "Dynamic carbon market driven multi-stage scheduling strategy for hydrogen integrated energy systems", *Renewable Energy*, pp. 125652, 2026.
[42] K. Taghizad-Tavana, M. Tarafdar-Hagh, S. Nojavan, M. Yasinzadeh, and M. Ghanbari-Ghalehjoughi, "Operation of smart distribution networks by considering the spatial–temporal flexibility of data centers and battery energy storage systems", *Sustainable Cities and Society*, vol. 114, pp. 105746, 2024.